

This is a self-archived version of an original article. This version may differ from the original in pagination and typographic details.

Author(s): Shen, Hui; Xu, Zhen; Wang, Lingzheng; Han, Ying-Zi; Liu, Xianhu; Malola, Sami; Teo, Boon K.; Häkkinen, Hannu; Zheng, Nanfeng

Title: Tertiary Chiral Nanostructures from C-H...F Directed Assembly of Chiroptical Superatoms

Year: 2021

Version: Accepted version (Final draft)

Copyright: © 2021 Wiley-VCH GmbH

Rights: In Copyright

Rights url: <http://rightsstatements.org/page/InC/1.0/?language=en>

Please cite the original version:

Shen, H., Xu, Z., Wang, L., Han, Y.-Z., Liu, X., Malola, S., Teo, B. K., Häkkinen, H., & Zheng, N. (2021). Tertiary Chiral Nanostructures from C-H...F Directed Assembly of Chiroptical Superatoms. *Angewandte Chemie*, 60(41), 22411-22416.
<https://doi.org/10.1002/anie.202108141>

A Journal of the Gesellschaft Deutscher Chemiker

Angewandte Chemie

GDCh

International Edition

www.angewandte.org

Accepted Article

Title: Tertiary Chiral Nanostructures from C-H...F Directed Assembly of Chiroptical Superatoms

Authors: Hui Shen, Zhen Xu, Lingzheng Wang, Ying-Zi Han, Xianhu Liu, Sami Malola, Boon K. Teo, Hannu Häkkinen, and Nanfeng Zheng

This manuscript has been accepted after peer review and appears as an Accepted Article online prior to editing, proofing, and formal publication of the final Version of Record (VoR). This work is currently citable by using the Digital Object Identifier (DOI) given below. The VoR will be published online in Early View as soon as possible and may be different to this Accepted Article as a result of editing. Readers should obtain the VoR from the journal website shown below when it is published to ensure accuracy of information. The authors are responsible for the content of this Accepted Article.

To be cited as: *Angew. Chem. Int. Ed.* 10.1002/anie.202108141

Link to VoR: <https://doi.org/10.1002/anie.202108141>

RESEARCH ARTICLE

Tertiary Chiral Nanostructures from C-H...F Directed Assembly of Chiroptical Superatoms

Hui Shen,^{+[a]} Zhen Xu,^{+[a]} Lingzheng Wang,^[a] Ying-Zi Han,^[a] Xianhu Liu,^[a] Sami Malola,^[b] Boon K. Teo,^{+[a]} Hannu Häkkinen,^{+[b]} and Nanfeng Zheng^{+[a]}

- [a] H. Shen, Z. Xu, L. Wang, Y. Z. Han, X. Liu, Prof. B. K. Teo, Prof. N. F. Zheng
State Key Laboratory for Physical Chemistry of Solid Surfaces, Collaborative Innovation Center of Chemistry for Energy Materials, and National & Local Joint Engineering Research Center for Preparation Technology of Nanomaterials, College of Chemistry and Chemical Engineering, Xiamen University
Xiamen 361005, China
E-mail: nfzheng@xmu.edu.cn; boonkteo@xmu.edu.cn
- [b] Dr. S. Malola, Prof. H. Häkkinen
Departments of Physics and Chemistry, Nanoscience Center, University of Jyväskylä
FI-40014 Jyväskylä, Finland
Email: hannu.j.hakkinen@jyu.fi
- [+] These authors contributed equally to this work.

Supporting information for this article is given via a link at the end of the document.

Abstract: Chiral hierarchical structures are universal in nature, whereas quite challenging to mimic in man-made synthesis. We report herein the synthesis and structure of tertiary chiral nanostructures with 100% optical purity. A novel synthetic strategy, using chiral reducing agent, *R* and *S*-BINAPCuBH₄ (BINAP is 2,2'-Bis(diphenylphosphino)-1,1'-binaphthyl), is developed to access to atomically precise, intrinsically chiral [Au₇Ag₆Cu₂(*R*- or *S*-BINAP)₃(SCH₂Ph)₆]⁺SbF₆⁻ nanoclusters in one-pot synthesis. The clusters represent the first trimetallic superatoms with inherent chirality and fair stability. Both metal distribution (primary) and ligand arrangement (secondary) of the enantiomers exhibited perfect mirror images, and unprecedentedly, the self-assembly driven by the C-H...F interaction between the phenyl groups of the superatom moieties and SbF₆⁻ anions induced the formation of bio-mimic *left*- and *right*-handed helices, achieving the tertiary chiral nanostructures. Density functional theory calculations revealed the connections between the molecular details and chiral optical activity.

Introduction

Chirality is a basic characteristic of nature, and can be observed at various hierarchical levels from subatomic and molecular to nanoscopic and galactic scales.^[1] One typical example is the hierarchical chiral structures of proteins, from basic component (amino acids), to the secondary structures (α -helix and β -sheet) and even proteases. Beyond that, creation of similar hierarchical chiral nanostructures from inorganic building blocks has been long pursued toward advanced functional materials.^[2] Although great progress has been made in recent decades in preparing and assembling chiral inorganic nanostructures, achieving hierarchical chiral arrangement is still a real challenge.^[3] Specifically, the creation of atomically uniform hierarchical chiral architectures with 100% optical purity and study of chirality origin at the molecular level remains a challenging task for most chiral nanostructures.^[4]

Atomically precise metal nanoclusters (NCs) provide a great opportunity to achieve and study hierarchical chiral

nanostructures.^[5] The nanostructures of NCs can be precisely determined through X-ray crystallographic technology.^[4b, 6] For example, recent reports by the groups of Zheng, Zang, Wang and Konishi demonstrated that metal clusters with 100% optical purity can be readily attained by employing chiral organic ligands.^[7] It has also been well documented that clusters can be assembled into larger nanostructures by virtue of ionic interaction between metal atoms and organic linkers.^[8] Furthermore, the work reported by Jin and Robinson for the observation of hierarchical complexity in thiolate-stabilized metal NCs and their assemblages nicely demonstrated their similarity to natural living systems.^[9]

It should be noted, however, that although chiral arrangement was observed in hierarchical nanostructures reported by Jin and Robinson, they were racemic in nature. Here, we report the synthesis and structure of the first tertiary chiral nanostructures with 100% optical purity. In this work, novel trimetallic chiral clusters, namely, [Au₇Ag₆Cu₂(*R*- or *S*-BINAP)₃(SCH₂Ph)₆]⁺, as the SbF₆⁻ salts, with 100% optical purity, were attained. Both metal framework (primary structure) and surface ligands (secondary structure) of the clusters exhibit chirality. Unprecedentedly, benefiting from the presence of SbF₆⁻ in the nanostructures, the *R*- and *S*-[Au₇Ag₆Cu₂(BINAP)₃(SCH₂Ph)₆]⁺ moieties were delicately assembled through C-H...F interaction to form the bio-mimic *left*- and *right*-handed helices (tertiary structure). Density functional theory (DFT) calculations revealed the details of counterion-cluster interactions as a strong driving force for chiral assembly and explained the optical activity in the molecular orbital basis.

Results and Discussion

Synthesis. The title clusters were synthesized from direct reduction of metal complexes by chiral reducing agents, *R*- and *S*-BINAPCuBH₄. The synthesis was inspired by our previous work of using (Ph₃P)₂CuBH₄ function as a mild reducing agent for the preparation of metal NCs.^[10] The particular reducing agents employed in this work were prepared by the ligand exchange

RESEARCH ARTICLE

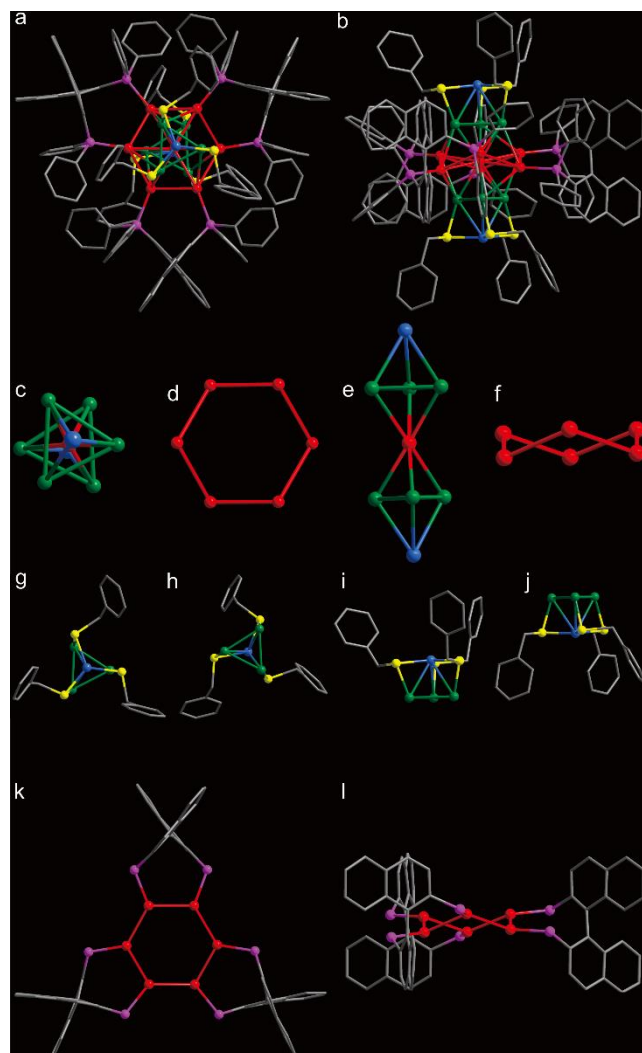


Figure 1. Structure of $\text{Au}_7\text{Ag}_6\text{Cu}_2(\text{R-BINAP})_3(\text{SCH}_2\text{Ph})_3$. (a-b) Total structure in top and side view. (c, e) The metal core can be viewed as fusion of two triangular bipyramids (CuAg_3Au) through sharing apex Au atom. (d, f) Chair conformation of the surrounding Au_6 belt. (g-j) The phenyl groups in the SCH_2Ph ligands are arranged clockwise or anti-clockwise at different ends of the cluster. (k-l) The arrangement of surface BINAP ligands. Color legend: red, Au; green, Ag; blue, Cu; pink, P; yellow, S; gray, C. All hydrogen atoms are omitted for clarity.

between *R* or *S*-BINAP and $(\text{Ph}_3\text{P})_2\text{CuBH}_4$ (Figure S1), using the synthetic protocol reported by Shubina *et al.*^[11]

In a typical synthesis, equal amounts of AuSCH_2Ph and AgSCH_2Ph polymers were added to mixture solvents of dichloromethane and methanol. Then a dichloromethane solution containing *R* or *S*-BINAPCuBH₄ was added consecutively under vigorous stirring. After aging for 12 hours, the solution was centrifuged and the brown-colored supernatant was subjected to vapor diffusion with ether. Brown block crystals were obtained after three weeks (Figure S2-3).

The clusters were first characterized by electrospray ionization mass spectrometry (ESI-MS) under positive ionization mode in CH_2Cl_2 . It showed a group of peaks in the range of 4600-5100 m/z , in which the dominant one corresponds to $[\text{Au}_7\text{Ag}_6\text{Cu}_2(\text{R-BINAP})_3(\text{SCH}_2\text{Ph})_6]^+$ (experimental m/z 4759.90, calculated m/z 4759.81) and other peaks are assigned to the species with metal exchanging (Figure S4). The proton-decoupling ^{31}P NMR of compound *R*- $\text{Au}_7\text{Ag}_6\text{Cu}_2$ shows a clear single peak at 23.62 ppm,

further verifying the spatial symmetry of the clusters (Figure S5-6).

Atomic structure. The crystalline products were then characterized by single-crystal X-ray crystallography at 100 K to be $[\text{Au}_7\text{Ag}_6\text{Cu}_2(\text{R- and S-BINAP})_3(\text{SCH}_2\text{Ph})_6]\text{SbF}_6$, designated hereafter as *R* or *S*- $\text{Au}_7\text{Ag}_6\text{Cu}_2$, respectively (Figure S7-10). The two crystals crystallize in chiral space groups of $P6_522$ (*R*- $\text{Au}_7\text{Ag}_6\text{Cu}_2$) and $P6_122$ (*S*- $\text{Au}_7\text{Ag}_6\text{Cu}_2$), respectively (Table S1 and S2). Shown in Figure 1a-1b and Figure S11 are the overall structure of *R*- $\text{Au}_7\text{Ag}_6\text{Cu}_2$ in two different views. For each cluster molecule, its metal core can be described as a two-capped trigonal antiprism ($\text{Cu}_2\text{Ag}_6\text{Au}$) with a single Au center or fusion of two CuAg_3Au triangular bipyramids through sharing an apex Au atom (Figure 1c and 1e). We note that the two triangular Ag_3 units are stacked in a non-perfect staggered fashion (Figure 1c and Figure S12). The distances within the $\text{Cu}_2\text{Ag}_6\text{Au}$ core indicate strong metal-metal bonding, as evidenced by the normal bond lengths listed in Table S3-4. The $\text{Cu}_2\text{Ag}_6\text{Au}$ core is surrounded by a Au_6 “belt” with chair conformation at the “equatorial” position (Figure 1d, 1f, detailed bond lengths see Table S3-4). Each Cu atom is coordinated by three thiolate ligands. The Cu atoms also bind with an Ag atom of the Ag_3 triangle (Figure 1g-j). Each surface Au atom is ligated by a phosphine atom from the bidentate BINAP ligands (Figure 1k-l).

The most interesting feature of the structure of the title clusters described above is its intrinsic chirality. Figure 2a portrays the metal cores of the two enantiomers, showing near perfect mirror images of *R*- $\text{Au}_7\text{Ag}_6\text{Cu}_2$ and *S*- $\text{Au}_7\text{Ag}_6\text{Cu}_2$ as determined by single-crystal X-ray crystallography. To the best of our knowledge, this is the first report of a tri-metallic cluster with 100% optical purity. The chirality is corroborated by the circular dichroism (CD) spectra (*vide infra*). Detailed analysis of the molecular architecture of *R*- $\text{Au}_7\text{Ag}_6\text{Cu}_2$ revealed that the naphthalene groups of chiral BINAP bind with Ag atoms via strong C-H \cdots Ag bonds (2.714 Å, Figure S13), thereby “locking in” the particular enantiomer and exerting the enantioselective control for the total metal framework (primary chiral structure). In turn, the chiral distribution of metal framework anti-react on the surface thiolates through strong Ag-S interactions, facilitating the “transfer” of the chirality of BINAPs to the thiolates (Figure 2b). Again, the C-H \cdots π interaction between thiolates and respective chiral BINAP ligands (Figure S13) forces the orientation of phenyl groups on mercaptan ligands to arrange in a propellar fashion. The arrangements of chiral BINAPs are also guided by the C-H \cdots π interaction between neighboring phosphine ligands (Figure S13-14). The chiral arrangement of both achiral thiolate and chiral phosphine ligands, thus, constitute the secondary chiral structure. In short, the existence of chiral BINAP ligands, as well as multiple hydrogen bonding and *van der Waals* interactions restrict the relative rotations of each component, thereby making the cluster molecule chiral.

Electronic structure. The electronic structure of $[\text{Au}_7\text{Ag}_6\text{Cu}_2(\text{R-BINAP})_3(\text{SCH}_2\text{Ph})_6]^+$ was computed through DFT (see details in SI text). Analysis of the Kohn-Sham orbitals indicates a fairly large energy gap (1.17 eV) between the HOMO and LUMO states. Internal charge distribution inside the cluster was analyzed by using the Bader method (Table S5) and it showed a strong electron donation from BINAP to Au, negative charge on thiolates and slight positive charge of Cu and Ag bound to thiolates.

RESEARCH ARTICLE

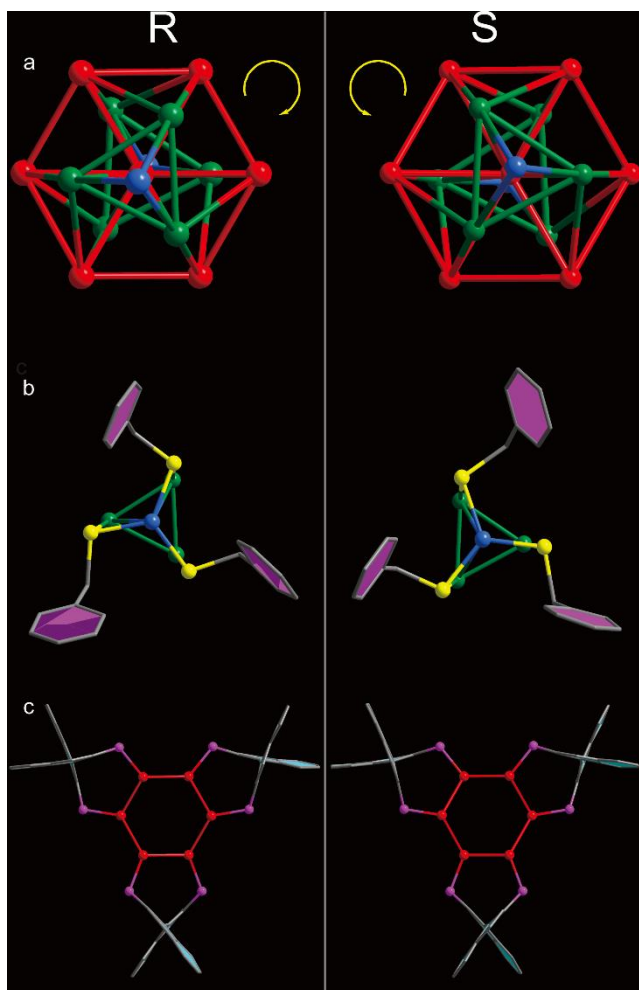


Figure 2. Anatomical representations of the two enantiomers of $\text{Au}_7\text{Ag}_6\text{Cu}_2$, $R\text{-Au}_7\text{Ag}_6\text{Cu}_2$ (left column) and $S\text{-Au}_7\text{Ag}_6\text{Cu}_2$ (right column). (a) Metal framework of two enantiomers exhibit clockwise and counterclockwise structure, respectively. (b) The propeller-like arrangements of the phenyl groups of the thiolates ligand. (c) Chiral arrangements of the surface BINAP ligands. Color legend: red, Au; green, Ag; blue, Cu; pink, P; yellow, S; gray, C. All hydrogen atoms are omitted for clarity.

Symmetry analysis and elemental decomposition of the frontier orbitals are shown in Figure S15. Overall, the cluster has a character of an 8-electron superatom as deduced from the electron counting rule,^[12] although the frontier orbital picture is rather complicated. There is a significant change in the orbital symmetry over the HOMO-LUMO energy gap, with the 5 lowest unoccupied states LUMO...LUMO+4 showing a dominant D symmetry in spherical harmonics about the cluster center-of-mass (Figure S15a). Dominant P symmetries are found for occupied states HOMO-4, HOMO-10, HOMO-11, and HOMO-12. As visualized in Figure S16 the frontier orbitals have a rich variation in localization at different parts of the cluster. The highest occupied states from HOMO-3 to HOMO are (2x2) degenerate and purely localized to the thiolate-metal interface, namely in the $\text{Cu}(\text{SR})_3$ protecting motifs at the poles of the cluster. Generally, two type of states are seen: i) flat horizontally oriented with phosphine-core localization and ii) prolate vertically oriented with thiolate-core localization. The vertically oriented thiolate-core states can be grouped based on degeneracy as HOMO-11, HOMO-9, {HOMO-8, HOMO-7} and {HOMO-6, HOMO-5},

HOMO-4 whereas horizontally oriented, phosphine-core states are seen in HOMO-13, HOMO-12, HOMO-10 and in all unoccupied states from LUMO to LUMO+10. The information about localization of the states is valuable for understanding the origin of the optical absorption and circular dichroism (CD) signals.

Optical and chiroptical response. As shown in Figure 3a, the CD spectra of the optically pure solution of R - and $S\text{-Au}_7\text{Ag}_6\text{Cu}_2$ display nearly perfect mirror-images signals from 250 to 600 nm. Specifically, $R\text{-Au}_7\text{Ag}_6\text{Cu}_2$ gave positive Cotton effects at 279, 358, 406, 465 and 482 nm with negative Cotton effects at 263 and 311 nm. Anisotropy factors $g=\Delta A/A$ were calculated over the spectral range and a maximum anisotropy factor of up to 0.52×10^{-3} at 313 nm was obtained (Figure 3b).

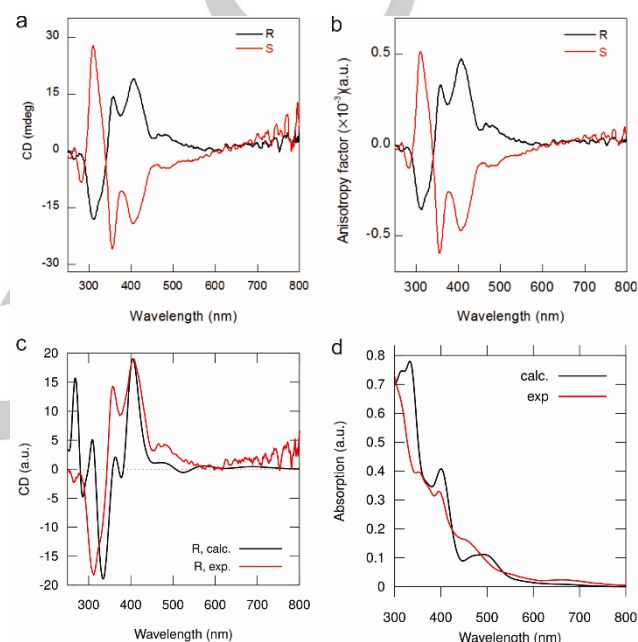


Figure 3. (a) Circular dichroism spectra of the enantiomers of chiral $\text{Au}_7\text{Ag}_6\text{Cu}_2$. (b) Corresponding anisotropy factors of R - and $S\text{-Au}_7\text{Ag}_6\text{Cu}_2$ enantiomers. Comparison of calculated and measured (c) CD spectra and (d) UV-vis absorption spectra of $R\text{-Au}_7\text{Ag}_6\text{Cu}_2$. Both computed spectra are blue-shifted by 0.55 eV to align the strongest positive CD peak at 406 nm. The intensity of the computed CD spectrum is scaled to measured intensity at 406 nm (c) and the intensity of the absorption spectrum (d) is scaled to the overall measured intensity in the UV-vis range. The computed spectra are obtained by broadening the individual oscillator and rotational strengths by 0.1 eV Gaussians.

UV-vis absorption and chiral response were investigated by using the linear response (LR) formulation of the time-dependent DFT (LR-TDDFT method, see details in the SI text). The measured UV-vis spectrum displays a weak tail below 700 nm, gradually rising elbows around 550 nm and 460 nm, and strong peaks around 400 nm and 350 nm. The computed spectrum is in a satisfactory agreement (Figure 3d) once a systematic underestimation of computed peak energies is corrected by applying a 0.55 eV blue-shift. The transitions were analyzed by using the so-called Dipole Transition Contribution Maps (DTCM) (Figure S17). DTCM analysis reveals that the P to D superatomic transitions are contributing to the absorption peaks up to 400 nm. The highest energy peak (333 nm) has various contributions from all parts of the cluster. The sharpest absorption peak at 400 nm is mainly related to specific transitions from Au-BINAP localized

RESEARCH ARTICLE

state HOMO-13 to Au-BINAP D-states LUMO and LUMO+1. These transitions have also an important role in the CD-spectrum as discussed next.

Table 1. Assignment between measured and computed positive (+) and negative (-) CD peaks (in nm) of $[\text{Au}_7\text{Ag}_6\text{Cu}_2(\text{R-BINAP})_3(\text{SCH}_2\text{Ph})_6]^{+}$. The computed values are given both with (comp1) and without (comp2) the 0.55 eV blueshift used in Figure 3c. The shift aligns the computed CD spectrum with the measured 406 nm positive peak (marked by *). ? = not observed.

exp	+/-	comp1	comp2
263	-	286	328
279	+	309	358
311	-	335	393
358	+	364	434
406*	+	406*	493
465	+	475	602
482	+	?	?
?	-	524	683
?	+	574	770

Comparison of the computed CD spectrum to the measured data shows that essentially all the measured positive and negative Cotton peaks can be assigned from theory (Figure 3c and Table 1). Contributions of individual electron-hole pairs, projected to different metals and ligands, to the computed peaks were done by using the so-called Rotatory strength Transition Contribution Maps (RTCM) and visualized in Figures S18 (lower energy peaks) and S19 (higher energy peaks). Of special interest are the two

strongest measured signals, a positive peak at 406 nm and a negative peak at 311 nm. The peak at 406 nm originates from a specific transition from HOMO-13 state to LUMO and LUMO+1 inside the chiral Au-BINAP "belt" (Figure S18). The peak at 311 nm has a mixed character. Holes are created both in the states of the aforementioned Au-BINAP "belt" and in the states in thiolates at both poles of the cluster, and electrons are transferred mainly to the first few empty states in the Au-BINAP belt (Figure S19). Thus, this transition involves strong interaction between both ligand types.

Chiral assembly in the crystal. Beside the ligand-induced chirality of individual clusters, the most surprising finding of the present study is the discovery of spontaneous self-assembly of the chiral metal clusters $\text{R-Au}_7\text{Ag}_6\text{Cu}_2$ and $\text{S-Au}_7\text{Ag}_6\text{Cu}_2$ to form optically pure helical chain nanostructures that crystallize in chiral space groups $P6_522$ ($\text{R-Au}_7\text{Ag}_6\text{Cu}_2$) and $P6_122$ ($\text{S-Au}_7\text{Ag}_6\text{Cu}_2$), respectively.

Crystal structure analysis showed that the arrangement and orientation of SbF_6^- anions in the unit cell play a key role in the self assembly of the chiral helical chains. It was found that there are multiple $\text{C-H} \cdots \text{F}$ hydrogen bonds between SbF_6^- and naphthalene groups of BINAP (2.787 Å) and phenyl groups of the thiolate (2.814 Å) ligands (Figure 4), suggesting the strong interactions between the clusters and the anions.^[13] DFT calculations were used to estimate the strength of the interactions between the cluster ion and the SbF_6^- counterion. Three complexes were cut out from the crystal structure and optimized by DFT. The attractive binding energy calculated per cluster / counterion interaction was found to be as follows: -2.03 eV for $[\text{Au}_7\text{Ag}_6\text{Cu}_2 / \text{SbF}_6]^{0}$, -1.90 eV for $[\text{Au}_7\text{Ag}_6\text{Cu}_2 / \text{SbF}_6 / \text{Au}_7\text{Ag}_6\text{Cu}_2]^{+}$, and -1.51 eV for $[\text{SbF}_6 / \text{Au}_7\text{Ag}_6\text{Cu}_2 / \text{SbF}_6]^{-}$. This is indicative of a rather strong interaction driving the stability of the chiral solid-state structure.

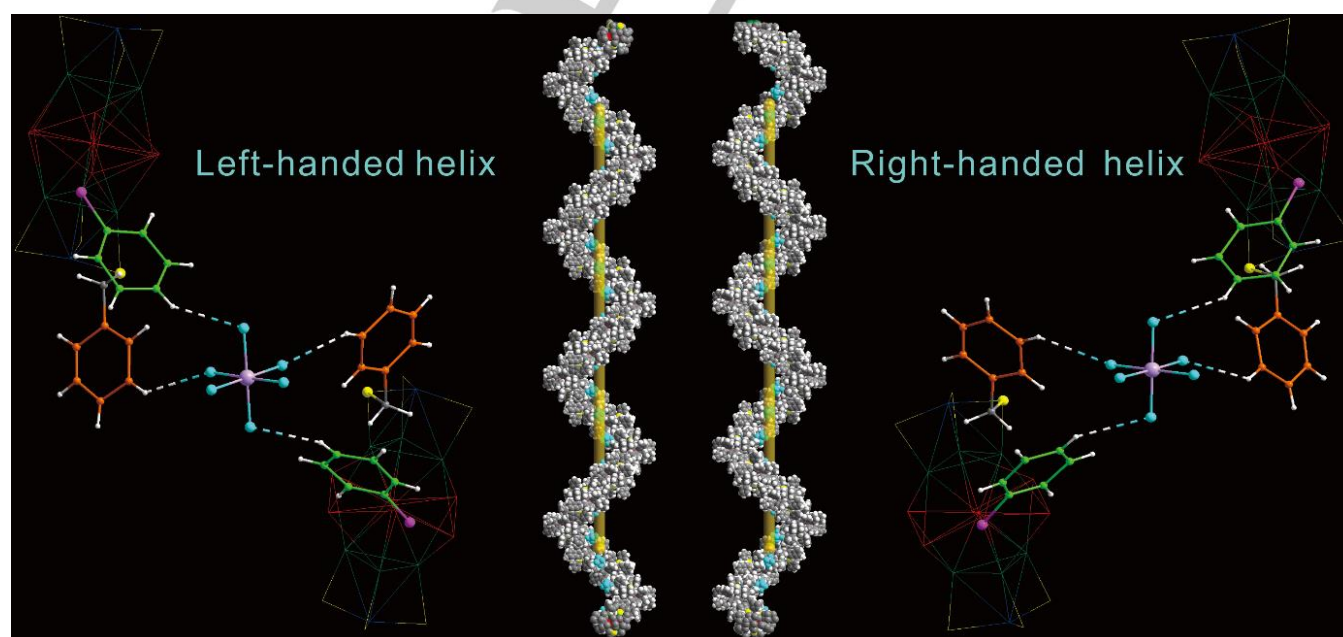


Figure 4. Packing diagram along b axis of R- and $\text{S-} [\text{Au}_7\text{Ag}_6\text{Cu}_2(\text{BINAP})_3(\text{SCH}_2\text{Ph})_3]\text{SbF}_6$ with intermolecular $\text{C-H} \cdots \text{F}$ hydrogen bonds, and *left* and *right*-handed helices formed. Color legend: red, Au; green, Ag; blue, Cu; pink, P; yellow, S; lavender, Sb; turquoise, F; gray, C; white, H.

RESEARCH ARTICLE

Further detailed structural analysis revealed that the cluster molecules are distributed as nodes along the *b*-axis in an organized manner, while SbF_6^- serves as a bridge to form a hexagonal net of helical chains (Figure S20). Specifically, one SbF_6^- links two clusters, in which two fluorine atoms in the para position form hydrogen bonds with thiol, and another two in the ortho position with phosphine ligands (Figure 4). There is a cavity made by fluorine atoms, with radius of $\sim 1.7\text{\AA}$ at the center of the assembled hexagonal framework (Figure S21). To our surprise, the simultaneous arrangement of the chiral clusters and the non-chiral SbF_6^- ions induce the formation of the chiral helical networks via hydrogen bonding. In detail, when $R\text{-Au}_7\text{Ag}_6\text{Cu}_2$ is present, a *left*-handed spiral is formed, and a *right*-handed one is constructed by using $S\text{-Au}_7\text{Ag}_6\text{Cu}_2$. Hydrogen bonds act as intermolecular driving forces to guide the formation of complex chiral assemblies, representing the tertiary chiral structure. We note that the quite similarity between α -helix of proteins and present helices strongly indicates that artificial self-assembly can reach the same level with biomolecules not only in terms of hierarchy, complexity and accuracy, but also chirality. Furthermore, this is the first time that $\text{C-H}\cdots\text{F}$ hydrogen bonding was observed to construct framework materials, albeit ionic^[14], covalent^[15], other hydrogen (including $\text{O}\cdots\text{H}$, and $\text{N}\cdots\text{H}$)^[16], and even halogen bonding^[17] were used in other works. Finally, we should note that the role(s) of simple inorganic ions, such as SbF_6^- , act more than just counterions, also protection units (by Mizuta)^[18] and framework linkers (by Zhu)^[8c]. The cluster is fairly stable, as UV-vis spectrum of the solution after storing under ambient conditions for one week did not change significantly (Figure S22), showing promise in the field of asymmetric catalysis, nonlinear optics, etc.

Conclusion

This work reports a novel and simple method for preparing chiral metal nanoclusters with 100% optical purity. It is hoped that the chiral reducing agents, *R*- and *S*-BINAPCuBH₄, can be used to afford other chiral metal clusters useful in asymmetric synthesis and catalysis and other chirality related fields in nanoscience and nanotechnology. Structural anatomy of present clusters, $[\text{Au}_7\text{Ag}_6\text{Cu}_2(\text{R- or S-BINAP})_3(\text{SCH}_2\text{Ph})_6]\text{SbF}_6$, clearly reveals the similarity of artificial nanostructures in the chiral complexity at different levels when compared with bio-structures. DFT computations characterized the cluster as a chiral 8 electron superatom where the ligand shell strongly affects the electronic structure and optical properties. In particular, the gold-phosphine framework around the “waist” of the cluster plays an important role affecting the chiroptical response in the CD spectrum. Geometrically, it serves as a primary structure like those defined as a biosystem (e.g., the chiral amino acids in a protein). The surface ligands, involving intrinsically chiral phosphines and achiral thiolates, all display chiral arrangement due to the multiple intramolecular interaction ($\text{C-H}\cdots\pi$), thus can be regarded to represent a secondary chiral structure (like chiral α -helix structure of a protein). Finally, the rare $\text{C-H}\cdots\text{F}$ hydrogen bonding as an intermolecular driving forces directs formation chiral helices, corresponding to a tertiary chiral structure, mimic to the chiral three-dimensional nanostructures of proteases. More work, involving expansion of the synthetic strategy, preparation of more framework materials through $\text{C-H}\cdots\text{F}$ hydrogen bonding, and

construction of nanostructures with more chiral levels, are ongoing.

Acknowledgements

We thank the National Key R&D Program of China (2017YFA0207302), the NNSF of China (21890752, 21731005, 21420102001, 21721001) and the 111 Project (B08027) for financial support. The computational work in the University of Jyväskylä was supported by the Academy of Finland through grants 292352, 315549, 319208. HH acknowledges support from China's National Innovation and Intelligence Introduction Base visitor program. The computations were made at the CSC supercomputing center in Finland.

Keywords: Chirality • Self-assembly • Cluster compounds • Hydrogen bonds • Hierarchical nanostructures

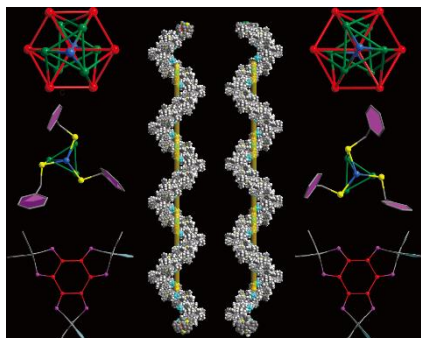
- [1] a) L. D. Barron, *Nature*, **2000**, 405, 895-896; b) H. B. Kolli, G. Cinacchi, A. Ferrarini, A. Giacometti, *Faraday Discuss.*, **2016**, 186, 171-186; c) C. Bai, M. Liu, *Angew. Chem. Int. Ed.*, **2013**, 52, 2678-2683.
- [2] a) K. Morisawa, T. Ishida, T. Tatsuma, *ACS Nano*, **2020**, 14, 3603-3609; b) H. Jiang, L. Zhang, J. Chen, M. Liu, *ACS Nano*, **2017**, 11, 12453-12460; c) A. Yuan, C. Hao, X. Wu, M. Sun, A. Qu, L. Xu, H. Kuang, C. Xu, *Adv. Mater.*, **2020**, 32, e1906580.
- [3] W. Ma, L. Xu, A. F. Moura, X. Wu, H. Kuang, C. Xu, N. A. Kotov, *Chem. Rev.*, **2017**, 117, 8041-8093.
- [4] a) B. Yeom, H. Zhang, H. Zhang, J. I. Park, K. Kim, A. O. Govorov, N. A. Kotov, *Nano Lett.*, **2013**, 13, 5277-5283; b) H. Shen, E. Selenius, P. Ruan, X. Li, P. Yuan, O. Lopez-Estrada, S. Malola, S. Lin, B. K. Teo, H. Hakkinen, N. F. Zheng, *Chem. Eur. J.*, **2020**, 26, 8465-8470; c) J. Ni, S. Liu, G. Hu, Y. Hu, Z. Lao, J. Li, Q. Zhang, D. Wu, S. Dong, J. Chu, C. W. Qiu, *ACS Nano*, **2021**, 15, 2893-2900.
- [5] a) R. Jin, C. Zeng, M. Zhou, Y. Chen, *Chem. Rev.*, **2016**, 116, 10346-10413; b) J. Yan, B. K. Teo, N. F. Zheng, *Acc. Chem. Res.*, **2018**, 51, 3084-3093; c) C. Sun, B. K. Teo, C. Deng, J. Lin, G. Luo, C. H. Tung, D. Sun, *Coord. Chem. Rev.*, **2021**, 427, 213576; d) Q. Yao, T. Chen, X. Yuan, J. Xie, *Acc. Chem. Res.*, **2018**, 51, 1338-1348; e) S. Sharma, K. K. Chakrahari, J. Saillard, C. W. Liu, *Acc. Chem. Res.*, **2018**, 51, 2475-2483; f) A. Ghosh, O. F. Mohammed, O. M. Bakr, *Acc. Chem. Res.*, **2018**, 51, 3094-3103; g) S. Takano, T. Tsukuda, *J. Am. Chem. Soc.*, **2021**, 143, 1683-1698; h) Z. Gan, N. Xia, Z. Wu, *Acc. Chem. Res.*, **2018**, 51, 2774-2783.
- [6] a) P. D. Jadzinsky, G. Calero, C. J. Ackerson, D. A. Bushnell, R. D. Kornberg, *Science*, **2007**, 318, 430-433; b) H. Yang, Y. Wang, H. Huang, L. Gell, L. Lehtovaara, S. Malola, H. Hakkinen, N. F. Zheng, *Nat. Commun.*, **2013**, 4, 2422; c) M. R. Narouz, K. M. Osten, P. J. Unsworth, R. W. Y. Man, K. Salorinne, S. Takano, R. Tomihara, S. Kaappa, S. Malola, C. T. Dinh, J. D. Padmos, K. Ayoo, P. J. Garrett, M. Nambo, J. H. Horton, E. H. Sargent, H. Hakkinen, T. Tsukuda, C. M. Crudden, *Nat. Chem.*, **2019**, 11, 419-425; d) H. Shen, G. Deng, S. Kaappa, T. Tan, Y. Z. Han, S. Malola, S. C. Lin, B. K. Teo, H. Hakkinen, N. F. Zheng, *Angew. Chem. Int. Ed.*, **2019**, 58, 17731-17735; e) Z. Zhu, J. Guo, W. Liu, Z. Li, B. Han, W. Zhang, Z. Tang, *Angew. Chem. Int. Ed.*, **2013**, 52, 13571-13575; f) H. Shen, Z. Xu, M. S. A. Hazer, Q. Wu, J. Peng, R. Qin, S. Malola, B. K. Teo, H. Hakkinen, N. F. Zheng, *Angew. Chem. Int. Ed.*, **2021**, 60, 3752-3758; g) S. Knoppe, T. Burgi, *Acc. Chem. Res.*, **2014**, 47, 1318-1326; h) I. Dolamic, B. Varnholt, T. Burgi, *Nat. Commun.*, **2015**, 6, 7117.
- [7] a) H. Yang, J. Yan, Y. Wang, G. Deng, H. Su, X. Zhao, C. Xu, B. K. Teo, N. F. Zheng, *J. Am. Chem. Soc.*, **2017**, 139, 16113-16116; b) G. Deng, S. Malola, J. Yan, Y. Han, P. Yuan, C. Zhao, X. Yuan, S. Lin, Z. Tang, B. K. Teo, H. Hakkinen, N. F. Zheng, *Angew. Chem. Int. Ed.*, **2018**, 57, 3421-3425; c) M. M. Zhang, X. Y. Dong, Z. Y. Wang, H. Y. Li, S. J. Li, X. Zhao, S. Q. Zang, *Angew. Chem. Int. Ed.*, **2020**, 59, 10052-10058; d) Y.

RESEARCH ARTICLE

- J. Kong, Z. P. Yan, S. Li, H. F. Su, K. Li, Y. X. Zheng, S. Q. Zang, *Angew. Chem. Int. Ed.*, **2020**, 59, 5336-5340; e) S. Li, Z. P. Yan, X. L. Li, Y. J. Kong, H. Y. Li, G. G. Gao, Y. X. Zheng, S. Q. Zang, *Adv. Sci.*, **2020**, 7, 2000738; f) J. Q. Wang, Z. J. Guan, W. D. Liu, Y. Yang, Q. M. Wang, *J. Am. Chem. Soc.*, **2019**, 141, 2384-2390; g) Y. Yanagimoto, Y. Negishi, H. Fujihara, T. Tsukuda, *J. Phys. Chem. B*, **2006**, 110, 11611-11614; h) M. Suguchi, Y. Shichibu, K. Konishi, *Angew. Chem. Int. Ed.*, **2018**, 57, 7855-7859.
- [8] a) M. Zhang, K. Li, S. Q. Zang, *Adv. Opt. Mater.*, **2020**, 8, 1902152; b) R. W. Huang, Y. S. Wei, X. Y. Dong, X. H. Wu, C. X. Du, S. Q. Zang, T. C. W. Mak, *Nat. Chem.*, **2017**, 9, 689-697; c) S. Chen, W. Du, C. Qin, D. Liu, L. Tang, Y. Liu, S. Wang, M. Zhu, *Angew. Chem. Int. Ed.*, **2020**, 59, 7542-7547.
- [9] a) C. Zeng, Y. Chen, K. Kirschbaum, K. J. Lambright, R. Jin, *Science*, **2016**, 354, 1580-1584; b) H. Han, Y. Yao, A. Bhargava, Z. Wei, Z. Tang, J. Suntivich, O. Voznyy, R. D. Robinson, *J. Am. Chem. Soc.*, **2020**, 142, 14495-14503.
- [10] H. Shen, Y. Han, Q. Wu, J. Peng, B. K. Teo, N. F. Zheng, *Small Methods*, **2020**, 10.1002/smt.202000603.
- [11] N. Belkova, I. Golub, E. Gutsul, K. Lyssenko, A. Peregodov, V. Makhaev, O. Filippov, L. Epstein, A. Rossin, M. Peruzzini, E. Shubina, *Crystals*, **2017**, 7, 318.
- [12] M. Walter, J. Akola, O. L. Acevedo, P. D. Jadzinsky, G. Calero, C. J. Ackerson, R. L. Whetten, H. Gronbeck, H. Häkkinen, *Proc. Natl. Acad. Sci.*, **2008**, 105, 9157-9162.
- [13] a) C. H. Chen, F. P. Gabbaï, *Angew. Chem. Int. Ed.*, **2017**, 56, 1799-1804; b) W. Yuan, H. Yang, C. Duan, X. Cao, J. Zhang, H. Xu, N. Sun, Y. Tao, W. Huang, *Chem*, **2020**, 6, 1998-2008; c) T. J. Barbarich, C. D. Rithner, S. M. Miller, O. P. Anderson, S. H. Strauss, *J. Am. Chem. Soc.*, **1999**, 121, 4280-4281.
- [14] a) A. Cadiou, K. Adil, P. M. Bhatt, Y. Belmabkhout, M. Eddaoudi, *Science*, **2016**, 353 137-140; b) H. C. Zhou, S. Kitagawa, *Chem. Soc. Rev.*, **2014**, 43, 5415-5418.
- [15] S. Kandambeth, K. Dey, R. Banerjee, *J. Am. Chem. Soc.*, **2019**, 141, 1807-1822.
- [16] a) P. S. Nugent, V. L. Rhodus, T. Pham, K. Forrest, L. Wojtas, B. Space, M. J. Zaworotko, *J. Am. Chem. Soc.*, **2013**, 135, 10950-10953; b) I. Hisaki, C. Xin, K. Takahashi, T. Nakamura, *Angew. Chem. Int. Ed.*, **2019**, 58, 11160-11170.
- [17] G. Cavallo, P. Metrangolo, T. Pilati, G. Resnati, M. Sansotera, G. Terraneo, *Chem. Soc. Rev.*, **2010**, 39, 3772-3783.
- [18] H. Shen, T. Mizuta, *Chem. Asian. J.*, **2017**, 12, 2904-2907.
- [19] CCDC 2096619 and 2096621 contain the supplementary crystallographic data for this paper. These data can be obtained free of charge from The Cambridge Crystallographic Data Centre.

RESEARCH ARTICLE

Entry for the Table of Contents



Tertiary chiral nanostructures have been created by assembling chiroptical superatoms of $[\text{Au}_7\text{Ag}_6\text{Cu}_2(\text{R- or S-BINAP})_3(\text{SCH}_2\text{Ph})_6]^+$ (BINAP = 2,2'-Bis(diphenylphosphino)-1,1'-binaphthyl). Both metal framework (primary structure) and surface ligands (secondary) of the nanocluster display perfect mirror symmetry. Extensive C-H \cdots F hydrogen bonding between the clusters and the SbF_6^- counteranions directed the formation of *left-* or *right-*handed helices, representing tertiary chiral nanostructure.